J. Fluid Mech. (2012), *vol.* 695, *pp.* 63–80.
doi:10.1017/jfm.2011.556

Three-dimensional river bed forms

M. Colombini† and A. Stocchino

Dipartimento di Ingegneria delle Costruzioni, dell'Ambiente e del Territorio, Università degli Studi di Genova, via Montallegro 1, 16145 Genova, Italy

(Received 4 October 2011; revised 4 October 2011; accepted 15 December 2011; first published online 7 February 2012)

The linear stability of a uniform flow in an infinitely wide erodible channel is investigated with respect to disturbances of the bed that are periodic in both the transverse and the longitudinal directions. A rotational flow and sediment transport model, originally developed to study the formation of two-dimensional dunes and antidunes, is straightforwardly extended to cover variations in the lateral direction. Sediment is assumed to be transported as bed load, disregarding the role of suspension. Following a standard linearization procedure, a dispersion relationship is obtained that expresses the growth rate and the celerity of the sand wave as a function of the streamwise and spanwise wavenumbers and of the relevant flow and sediment parameters. Regions of instabilities in the space of the parameters are found, which can be associated with bed forms of different kinds, spanning from dunes and antidunes to alternate bars. Therefore, the present theory allows for a unified view of the formation of two- and three-dimensional bed forms in rivers in terms of the relevant flow and sediment parameters.

Key words: river dynamics, sediment transport

1. Introduction

River bed forms are commonly classified in terms of their characteristic longitudinal scales: the sediment grain size for ripples; the flow depth for dunes and antidunes; the channel width for bars. The distinction of bed patterns into micro-, meso- and macro-forms dates back to the first geomorphological observations (see Allen 1982 for a comprehensive review) and guided both experimental and theoretical researches in this field in the last century. Thus notwithstanding, it is clear that the formation of river patterns is driven by the same basic mechanism so that such a neat separation among different bed forms should not always be expected to hold when the relevant flow and sediment parameters are varied continuously. Moreover, though laboratory experiments are carefully designed to isolate a single type of bed form from the others, bed patterns often arise that are not easily classified in terms of the above schematic categories. The situation is even more complex when three-dimensionality is considered, since several transverse modes can be identified, depending on the integer ratio between the channel width and (half) the transverse wavelength. A typical example involves alternate and central bars, which are associated with the first and the

† Email address for correspondence: col@dicat.unige.it

second transverse modes, respectively. Note, however, that a similar behaviour can be expected also for three-dimensional dunes, the first transverse mode of which being associated with a diagonal pattern that can be easily confused with alternate bars.

For these reasons, predicting which particular bed pattern will arise, for any given set of the relevant flow and sediment parameters, among the variety of possible configurations, is indeed a challenging task. In this regard, linear analyses are known to provide a deep insight into the mechanism that drives bed form instability, being able to identify regions in the space of the parameters where bed forms are expected to form and to show how the onset of the instability is controlled by some relevant parameters (e.g. the width-to-depth ratio for bars, the Froude number for dunes and antidunes). Moreover, the role of some parameters in inducing a transition between different types of bed forms can be made evident. Despite this fact, the formation of meso- (e.g. dunes and antidunes) and macro-forms (e.g. bars) has been seldom investigated in the past in the same framework of linear instability.

Indeed, as a simple glance at the linearized form of the Exner equations reveals, instability is the result of a subtle balance between the effect of the bed shear stress, which may be either destabilizing or stabilizing depending on its lag with respect to the bed profile, and the stabilizing effect of gravity, which acts in both the streamwise and spanwise directions. Several effects can be added to this basic mechanism (e.g. suspension, sorting, sediment inertia), which, however, stands out for its simplicity and effectiveness in describing flow–bed interactions. Therefore, in the following, attention is focused on the simple case of a well-sorted sediment mixture, characterized by its median diameter and moving as bedload only. Moreover, hydraulically rough conditions are assumed for the turbulent flow, so that ripple formation (Colombini & Stocchino 2011) is excluded by the present analysis, and the quasisteady approximation is adopted, whereby time derivatives are neglected in flow equations. It is clear that, under these conditions, the ability of the flow model to predict the ‘correct’ lag becomes crucial.

In the decade that followed the work of Kennedy (1963), the formation of two- and three-dimensional bed forms was extensively investigated by means of linear stability analyses. On the basis of the flow model used, these works were grouped by Reynolds (1976) into three main categories: potential-flow, shallow-water (or ‘hydraulic’) and rotational solutions. Although these analyses were successful in describing some of the features that characterize the formation of bed forms, a comprehensive view of the process was lacking, mainly due to the intrinsic limitation of the flow models adopted. On one hand, potential-flow models provide no bed shear stress, so that a lag must be introduced to give rise to instability, either artificially or by invoking the presence of suspension, which is, however, negligible at low values of the Shields parameter. On the other hand, shallow-water models, which account for friction, are limited in application to processes which occur over streamwise distances many times greater than the flow depth. As a result, they can successfully describe alternate bar formation (Callander 1969; Blondeaux & Seminara 1985; Colombini, Seminara & Tubino 1987; Tubino, Repetto & Zolezzi 1999; Hall 2006) but cannot handle the dynamics of dunes and antidunes, the wavelength of which scales with flow depth, equally well. In particular, long two-dimensional waves are found to be unstable only for Froude numbers larger than 2, a condition that corresponds to the formation of roll waves over a fixed plane bed (Gradowczyk 1968). Shallow-water models have also been used to study the formation of tidal sand banks in shallow seas (Idier & Astruc 2003; Roos *et al.* 2004).

Rotational flow models can, in principle, encompass the above limitations, thus providing a more accurate description of the bed shear stress. Making use of a simple rotational flow model, based on a constant eddy viscosity and on a slip-velocity approach, Engelund (1970) and Fredsøe (1974*b*) were able to provide the first stability theories for dune and antidune formation. With the same flow model, they also investigated the development of three-dimensional 'oblique' dunes (Engelund 1974; Fredsøe 1974*a*). However, in their analyses, the transition from lower- to upper-regime bed forms is shown to be controlled by a delicate balance between suspended load and bedload (Engelund & Fredsøe 1974). In the limiting case of negligible bedload only antidunes form, whereas with negligible suspended load dunes form, but no stabilizing mechanism is present to damp antidune instability in the short-wavelength range, the effect of gravity being relevant only for low values of the Shields parameter. Since the transition from dunes to antidunes is likely to be controlled by the Froude number alone, a consistent picture of dune and antidune formation was still lacking. More recently, Colombini (2004) showed that such a picture is indeed contained in the simple framework of instability considered, provided the bedload layer thickness is accounted for in the analysis. The latter theory is here extended to the third dimension, aiming at the investigation of the effects associated with three-dimensionality in the formation of bed forms. In this regard, the analyses of Besio, Blondeaux & Vittori (2006) and Blondeaux & Vittori (2011), who adopted a three-dimensional model to study the formation of tidal sand waves and sand banks in shallow seas and of dunes and bars in tidal channels, are worth noting.

Finally, it must be noted that several investigations have recently been conducted on the formation of two- and three-dimensional bed forms under laminar flow conditions. Although laminar-flow analogues of turbulent-flow morphologies cannot and should not be expected to satisfy dynamic similarity in terms of all relevant dimensionless parameters (Lajeunesse *et al.* 2010), yet similar configurations of the bed morphology are often observed, irrespective of the turbulent or laminar character of the flow, thus suggesting that they may have a common physical ground. In particular, we would like to mention the recent work of Devauchelle *et al.* (2010), who investigated the role of three-dimensionality in the formation of laminar-flow bed forms and described a ripple–bar transition which presents strong similarities with the dune–bar transition described in the following.

2. Experimental observations

Before entering into the details of the present theoretical analysis, it may be useful to discuss experimental observations on two- and three-dimensional bed forms in order to enlighten their main morphological features, namely the streamwise and spanwise characteristic wavenumbers, and the role played by the relevant flow and sediment parameters.

To this end, the collection of flume experiments concerning dunes and antidunes of Guy, Simons & Richardson (1966), denoted in the following as GSR, has been integrated with a data set, denoted as JSM, composed by the sand experimental runs extracted from Sukegawa (1971), Muramoto & Fujita (1978) and Jaeggi (1984). These runs have been selected among others since a clear distinction was made between alternate and diagonal bars, the latter being shorter bars that develop for low values of the width-to-depth ratio, when the Froude number is close to unity. Later on, this distinction will be discussed in more detail, since we argue that diagonal bars should be considered as the first transverse mode of instability of three-dimensional dunes.

Following a well-established procedure, results from both data sets, which have been collected at the end of the experiments and are therefore relative to mature bed forms, have been processed to eliminate the effects of form resistance and sidewalls, by searching for the equivalent uniform flow that exerts the same shear stress on the bed and is characterized by the same depth-averaged velocity U^* (a star superscript identifies dimensional variables). A non-dimensional Chézy coefficient C is then introduced that relates U^* to the friction velocity of the bed region u_b^* and to the corresponding hydraulic radius r_b^* through the Keulegan equation (ASCE, Task Committee 1963) valid for the rough regime:

$$C = \frac{U^*}{u_b^*} = \frac{1}{\kappa} \ln\left(\frac{11.09 r_b^*}{2.5 d^*}\right), \tag{2.1}$$

where κ is the Von Kármán constant, taken as 0.4, and the roughness height has been set equal to 2.5 times the sediment diameter d^*. The above procedure allows for the implicit determination of the conductance coefficient C and, in turn, of u_b^* and r_b^*, the latter being equivalent to the uniform flow depth D^* in the infinitely wide configuration considered herein.

Among the relevant flow and sediment parameters, we recall the Froude number Fr, the Shields parameter θ, the non-dimensional grain size d_s and the width-to-depth ratio β, here defined with the half-width of the channel W_h^* as in previous studies on bar formation:

$$Fr = \frac{U^*}{\sqrt{gD^*}}, \quad \theta = \frac{u_b^{*2}}{(s-1)gd^*}, \quad d_s = \frac{d^*}{D^*}, \quad \beta = \frac{W_h^*}{D^*}, \tag{2.2}$$

where g is the gravitational acceleration and s is the relative density of the sediment, taken as 2.65. It is worth noting that, by virtue of (2.1), C can be considered as an alias of d_s and, accordingly, θ, Fr and C are interrelated:

$$\theta = \frac{Fr^2}{(s-1)d_s C^2} \simeq 0.14 Fr^2 \frac{\mathrm{e}^{\kappa C}}{C^2}. \tag{2.3}$$

Moreover, for a uniform flow, the bed slope S is related to C and Fr by the well-known relationship

$$S = \frac{Fr^2}{C^2}. \tag{2.4}$$

In figure 1(*a*), the experimental runs of the JSM and GSR data sets are presented in the plane $(C, \theta/\theta_C)$, where θ_C is the critical value for incipient motion of the sediment. Even though the two data sets do not completely overlap (there is a small gap around $C = 15$ or $d_s = 0.01$), for relatively low values of the Shields parameter a clear tendency is shown for dunes to be replaced by bars as the conductance coefficient is lowered (and so for either shallower flows or coarser sediments). On the contrary, antidune runs are less sensitive to variation in C, being consistently present in both data sets down to a value of C of $\sim$10. The solid line in the plot is given by (2.3) with $Fr = 1$ and marks the boundary between the sub- and supercritical regimes for a long wave. It should be noted that the region bounded by this curve and the no-transport threshold, which represents subcritical flows with active transport, tends to contract as C is decreased. Moreover, dunes and antidunes are shown to belong to the sub- and supercritical regimes, respectively, indicating that the Froude number controls the onset of both instabilities. On the contrary, bars are shown to be quite insensitive to

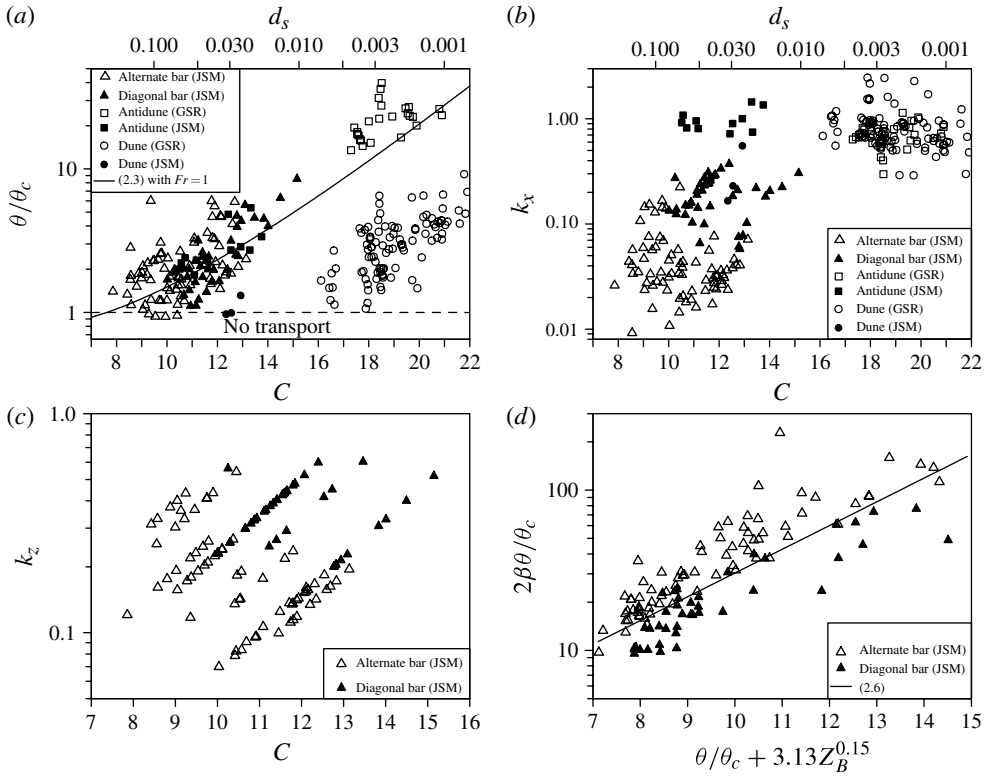

FIGURE 1. Experiments from JSM and GSR data sets: (*a*) the Shields parameter θ/θ_C versus the conductance coefficient C; the longitudinal (*b*) and transverse (*c*) wavenumbers k_x and k_z versus C; (*d*) Jaeggi's (1984) criterion for alternate bar formation.

the value of the Froude number, thus suggesting that another parameter (namely the width-to-depth ratio) should be considered as the relevant one for bar formation.

Bars can be better distinguished into alternate and diagonal in terms of the longitudinal and transverse wavenumbers, defined as

$$k_x = \frac{2\pi D^*}{L_x^*}, \quad k_z = \frac{2\pi D^*}{L_z^*} = \frac{2\pi D^*}{4W_h^*} = \frac{\pi}{2\beta}, \tag{2.5}$$

where L_x^* and L_z^* are the wavelengths in the streamwise and spanwise directions, respectively. Note that alternate and diagonal bars are both characterized by a transverse wavelength that is twice the channel width, so that k_z is inversely proportional to the width-to-depth ratio β.

In terms of the longitudinal wavenumber k_x, presented in figure 1(*b*), diagonal bars are shown to be much shorter than alternate bars, their characteristic wavenumber ($\sim$0.2) being about one order of magnitude larger than the one for alternate bars ($\sim$0.02), while still smaller than the one for dunes and antidunes ($\sim$1). Diagonal bars are also consistently shorter than alternate bars in the lateral direction, as shown in figure 1(*c*), being characterized by larger transverse wavenumbers k_z (and so by smaller width-to-depth ratios β) than alternate bars.

The distinction between diagonal and alternate bars was firstly proposed by Einstein & Shen (1964), who observed that diagonal bars are: "a special case of the diagonal

dune pattern, which occurs when the Froude number of the flow is nearly unity, at certain depth-to-width ratios. This pattern probably results from the water surface disturbance, since the diagonal bars oscillated transversely with the wave velocity of water depth and the entire bed pattern travels rapidly downstream with the flow".

In his experimental work, Jaeggi (1984) remarked that diagonal bars did not satisfy his proposed criterion for alternate bar formation, namely

$$2.93 \log\left(\frac{\theta}{\theta_C} 2\beta\right) \geqslant \frac{\theta}{\theta_C} + 3.13 Z_B^{0.15}, \tag{2.6}$$

where Z_B is the ratio between the channel width and the grain diameter. This is shown in figure 1(*d*), which is a remake of the original figure 3 of Jaeggi (1984). The solid line in the plot represents the threshold that bounds the alternate bar region as provided by (2.6). Enlightening the distinction between these two similar bed morphologies, he also observed that: "a grouping of three-dimensional mesoforms, in which the fronts of the mesoforms were diagonally aligned over the channel width, was responsible for the appearance of this feature". Note that, in the context of the paper, the word 'mesoform' was used to distinguish bed forms scaling with flow depth (i.e. dunes and antidunes) from those scaling with channel width (i.e. bars).

Therefore, experimental observations suggest that diagonal bars can be considered as intermediate bed forms associated with the transition of dunes from two- to three-dimensional configurations. Alternatively, diagonal bars can be thought of as the results of the influence of the flow depth (and thus of the Froude number) on alternate bars.

In the following, it will be shown that the present analysis satisfactorily accounts for most of the experimental observations presented above, namely: (i) the transition from two-dimensional dunes to alternate bars as the conductance coefficient is lowered at low values of the Shields parameter; (ii) the coexistence of bars and antidunes as the Shields parameter is raised at low values of the conductance coefficient; (iii) the interpretation of diagonal bars as three-dimensional oblique dunes, distinct from alternate bars.

3. Formulation of the problem

Let us consider a uniform turbulent free-surface flow in an infinitely wide channel. The triplet composed by the fluid density ρ, the bed friction velocity u_b^* and the flow depth D^* is used for non-dimensionalization.

In the sloping Cartesian coordinate system (x, y, z), sketched in figure 2, the dimensionless steady Reynolds and continuity equations read

$$UU_{,x} + VU_{,y} + WU_{,z} + P_{,x} - SC^2/Fr^2 - T_{xx,x} - T_{xy,y} - T_{xz,z} = 0, \tag{3.1}$$

$$UV_{,x} + VV_{,y} + WV_{,z} + P_{,y} + C^2/Fr^2 - T_{xy,x} - T_{yy,y} - T_{yz,z} = 0, \tag{3.2}$$

$$UW_{,x} + VW_{,y} + WW_{,z} + P_{,z} - T_{xz,x} - T_{yz,y} - T_{zz,z} = 0, \tag{3.3}$$

$$U_{,x} + V_{,y} + W_{,z} = 0, \tag{3.4}$$

where $\boldsymbol{U} = (U, V, W) = \{u_i\}$ is the velocity vector averaged over turbulence, P is the pressure and $\boldsymbol{T} = \{T_{ij}\}$ is the Reynolds stress tensor.

The flow domain is bounded by the curves $y = R(x, z, t)$ and $y = R(x, z, t) + D(x, z, t)$, where D is the local flow depth. The lower boundary is set at the reference level R, where the velocity is assumed to vanish. Having denoted as $\boldsymbol{n}$, $\boldsymbol{t}$ and $\boldsymbol{b}$ the unit vectors normal, tangential and binormal to each boundary, respectively, the kinematic and

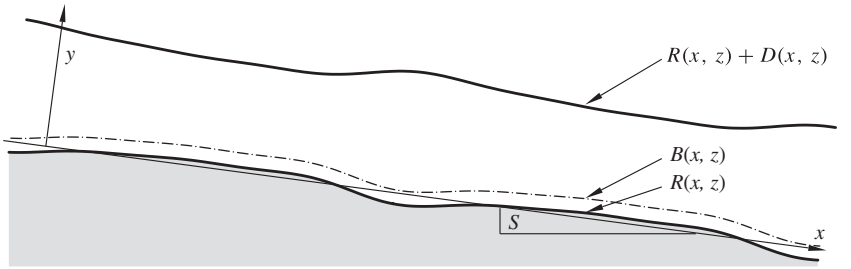

FIGURE 2. Sketch of a longitudinal section of the flow configuration. The z-axis extends out of the page.

dynamic boundary conditions to be associated with (3.1)–(3.4) read

$$\left.\begin{aligned} -R_{,t} + \boldsymbol{U}\cdot\boldsymbol{n} &= 0 \\ \boldsymbol{U}\cdot\boldsymbol{t} &= 0 \\ \boldsymbol{U}\cdot\boldsymbol{b} &= 0 \end{aligned}\right\} (y = R), \qquad \left.\begin{aligned} -(R+D)_{,t} + \boldsymbol{U}\cdot\boldsymbol{n} &= 0 \\ \boldsymbol{n}\cdot\boldsymbol{T}\cdot\boldsymbol{t} &= 0 \\ \boldsymbol{n}\cdot\boldsymbol{T}\cdot\boldsymbol{n} &= 0 \\ \boldsymbol{n}\cdot\boldsymbol{T}\cdot\boldsymbol{b} &= 0 \end{aligned}\right\} (y = R + D). \tag{3.5}$$

In order to close the above formulation, the Boussinesq closure is used, which reads

$$T_{ij} = \nu_T (u_{i,j} + u_{j,i}). \tag{3.6}$$

The eddy viscosity ν_T is evaluated by means of the mixing length approach; hence,

$$\nu_T = l^2 \left[(u_{i,j} + u_{j,i})u_{i,j}\right]^{1/2}, \quad l = \kappa(y - R + R_0 D)\left(\frac{D + R - y}{D}\right)^{1/2}. \tag{3.7}$$

Equation (3.7) provides, for a uniform flow, a parabolic profile for the eddy viscosity and, consequently, the logarithmic law of the wall, with R_0 being the dimensionless distance between the reference level and the average bed level.

The system (3.1)–(3.4) is complemented by the Exner equation imposing mass conservation of sediments, which takes the dimensionless form

$$B_{,t} - Q(\Phi_{Bx,x} + \Phi_{Bz,z}) = 0, \quad Q = \frac{d_s}{(1 - p_s)\sqrt{\theta}}, \tag{3.8}$$

where B represents the interface between the clear fluid and the bed load layer and p_s is the sediment porosity.

The intensity of the sediment load is then related to the local value of the Shields parameter through the classical Meyer-Peter & Müller (1948) formula

$$\Phi = A_m (\theta_B - \theta_C)^{3/2}, \quad \theta_B \geqslant \theta_C, \tag{3.9}$$

where θ_C is the critical Shields stress for incipient motion. The values of θ_C and A_m have been set equal to 0.0495 and 3.97, respectively, in accordance with the corrections proposed by Wong & Parker (2006) in their revisitation of the work of Meyer-Peter & Müller (1948). In addition, the effect of gravity in the longitudinal direction is included by reducing the critical Shields stress by an amount proportional to the local longitudinal slope:

$$\theta_C = 0.0495 - \mu_x(S - R_{,x}), \tag{3.10}$$

where μ_x is a dimensionless empirical constant set equal to 0.1 after Fredsøe (1974*b*). Note that only a few data points fall below the dashed line that bounds the no-transport region in figure 1(*a*), thus confirming the validity of this assumption for the experimental data sets considered.

Furthermore, the local direction of the sediment load is associated with an averaged direction of particles, which deviates from the direction of the local bed shear stress under the action of gravity. Following Engelund (1981), this correction has been assumed to be proportional to the local transverse slope and inversely proportional to the square root of the local value of the Shields parameter:

$$(\Phi_{Bx}, \Phi_{Bz}) = \Phi_B(\cos\delta, \sin\delta), \quad \sin\delta = \left(\frac{T_{Bxz}}{\sqrt{T_{Bxy}^2 + T_{Bxz}^2}} - \frac{\mu_z}{\sqrt{\theta_B}} R_{,z} \right), \tag{3.11}$$

where the coefficient μ_z has been set equal to 0.1. Note that a larger value (0.3) was adopted in Colombini *et al.* (1987) for the study of bars. The present choice has been found to slightly improve the comparison with experimental observations and can be theoretically justified in terms of the increase of the gravity coefficient $\mu_z/\sqrt{\theta_B}$ associated with its evaluation at the top of the bedload layer ($\theta_B < \theta$).

It must be stressed that the action of gravity has been modelled in a simplified way, strictly valid only for small lateral and longitudinal slopes, a situation that, however, pertains to the linear context analysed (Seminara, Solari & Parker 2002).

Indeed, the sediment transport model adopted is a straightforward extension to the third dimension of the model first presented in Colombini (2004) for the study of two-dimensional dunes and antidunes and slightly modified in subsequent works (Colombini & Stocchino 2005, 2008).

It might be useful to recall here that, in this model, all the quantities relevant for the sediment transport are evaluated at the interface B between the clear water and the bedload layer. By definition, the distance between the surface B and the actual bed R (where the flow velocity vanishes) is the thickness of the bedload layer L. The latter is assumed equal to the averaged maximum saltation height of the sediment h_s, which, in turn, depends on the Shields parameter by an empirical relationship that reads

$$L = B - R = (1 + h_s)d_s + 0.2d_s, \quad h_s = 1.42\left[\frac{\theta(1-L)}{\theta_C} - 1\right]^{0.64}. \tag{3.12}$$

Note that a few modifications have been introduced in (3.12) with respect to the analogous relationships of Colombini & Stocchino (2008). Firstly, the term $0.2d_s$, which accounts for the distance between the top of the grains and the average bed level for a three-dimensional packed set of spheres, was previously set equal to its two-dimensional counterpart, namely $d_s/6$. Secondly, the effective Shields stress used for the computation of h_s is set equal to $\theta(1-L)$, which, for the base uniform flow, corresponds to the Shields stress evaluated at the level B, consistently with the general formulation of the sediment transport model. This ultimately results in an implicit evaluation of the bedload layer thickness L through (3.12), which was not necessary in the previous model.

Finally, the following transformation of variables:

$$\eta = \frac{y - R(\xi, \zeta, \tau)}{D(\xi, \zeta, \tau)}, \quad \xi = x, \quad \zeta = z, \quad \tau = t \tag{3.13}$$

is employed to map the domain shown in figure 2 into a rectangular domain.

4. Linear analysis

The problem is solved in terms of normal modes, expanding a generic quantity G as

$$G(\xi, \eta, \tau) = G_0(\eta) + \epsilon G_1(\eta) \exp[\mathrm{i}k_x(\xi - \Omega\tau)] \exp[\mathrm{i}k_z\zeta] + \text{c.c.}, \tag{4.1}$$

where ϵ is a small parameter and Ω is the wave complex celerity.

Substituting the above expansion into the governing equations, boundary conditions and turbulence closure and collecting terms of the same order of magnitude in ϵ, the following differential problems arise. Note that, for convenience, the tangential (T_t), binormal (T_b) and normal (T_n) components of the stress acting on surfaces at constant η are introduced below, the latter including the role of pressure.

4.1. $O(\epsilon^0)$

At leading order, integration of the system of differential equations yields a linear distribution of the shear stress and the classical velocity logarithmic law:

$$U_0 = \frac{1}{\kappa} \ln\left(\frac{\eta + R_0}{R_0}\right) \tag{4.2}$$

and, by direct integration, the depth-averaged speed is obtained:

$$\overline{U}_0 = \frac{U^*}{u_f^*} = C = \frac{1}{\kappa}\left[\ln\left(\frac{1 + R_0}{R_0}\right) - 1\right], \tag{4.3}$$

which can be used to relate the coefficient C to R_0. Consistently with (2.1), the distance R_0 of the reference plane from the average bed elevation is found to be roughly equal to one-thirtieth of the non-dimensional roughness height or, alternatively, to one-twelfth of the non-dimensional sediment diameter d_s.

The eddy viscosity associated with the base flow reads

$$\nu_{T0} = l_0^2 U_0', \quad l_0 = \kappa(\eta + R_0)(1 - \eta)^{1/2}, \tag{4.4}$$

where primes stand for derivatives with respect to η.

The Exner equation (3.8) does not provide any additional information, since, under uniform flow conditions, the bed experiences neither aggradation nor degradation. The following relationships hold:

$$\theta_0 = \frac{C^2}{(s-1)d_s Fr^2}, \quad \theta_{B0} = \theta_0(1 - L_0), \quad \theta_{C0} = 0.0495 - \mu\frac{C^2}{Fr^2}, \tag{4.5}$$

$$\Phi_{B0} = 3.97\,(\theta_{B0} - \theta_{C0})^{3/2}, \quad Q = \frac{d_s}{(1 - p_s)\sqrt{\theta_0}}, \tag{4.6}$$

where the bedload layer thickness L_0 is obtained implicitly from (3.12):

$$L_0 = B_0 - R_0 = (1 + h_{s0})d_s + 0.2d_s, \quad h_{s0} = 1.42\left[\frac{\theta_0(1 - L_0)}{\theta_{C0}} - 1\right]^{0.64}. \tag{4.7}$$

Finally, the following quantities, to be used later on, are introduced:

$$A_{x0} = \frac{3}{2}\frac{\Phi_{B0}\theta_0}{\theta_{B0} - \theta_{C0}}, \quad A_{z0} = \frac{\Phi_{B0}\theta_0}{\theta_{B0}}, \quad A_{L0} = \frac{0.64 h_{S0} d_s}{\theta_{B0} - \theta_{C0}}. \tag{4.8}$$

4.2. $O(\epsilon^1)$

At the linear level, after some manipulations, a system of ordinary differential equations for the unknown vector $\boldsymbol{Z}_1 = (U_1, V_1, W_1, T_{t1}, T_{n1}, T_{b1})^{\mathrm{T}}$ is eventually

obtained and can be written in the general form

$$\mathscr{L}\mathbf{Z}_1 = D_1\boldsymbol{D}_1 + R_1\boldsymbol{R}_1, \tag{4.9}$$

where D_1 and R_1 represent the amplitudes of the perturbations of the flow depth and of the bed, respectively.

The linear differential operator $\mathscr{L}$ in (4.9) reads

$$\mathscr{L} = \begin{pmatrix} d/d\eta & \mathrm{i}k_x & 0 & -1/(2\nu_{T0}) & 0 & 0 \\ \mathrm{i}k_x & d/d\eta & \mathrm{i}k_z & 0 & 0 & 0 \\ 0 & \mathrm{i}k_z & d/d\eta & 0 & 0 & 1/\nu_{T0} \\ \mathscr{L}_{41} & -U_0' & -3k_xk_z\nu_{T0} & d/d\eta & \mathrm{i}k_x & 0 \\ 0 & -\mathrm{i}k_xU_0 & 0 & \mathrm{i}k_x & d/d\eta & \mathrm{i}k_z \\ -3k_xk_z\nu_{T0} & 0 & \mathscr{L}_{63} & 0 & \mathrm{i}k_z & d/d\eta \end{pmatrix}, \tag{4.10}$$

where

$$\mathscr{L}_{41} = -\mathrm{i}k_xU_0 - (4k_x^2 + k_z^2)\nu_{T0}, \quad \mathscr{L}_{63} = -\mathrm{i}k_xU_0 - (k_x^2 + 4k_z^2)\nu_{T0}. \tag{4.11}$$

The vectors $\boldsymbol{D}_1$ and $\boldsymbol{R}_1$ are, respectively,

$$\boldsymbol{D}_1 = \begin{pmatrix} 0 \\ \mathrm{i}k_xU_0'\eta \\ 0 \\ -\mathrm{i}k_xU_0U_0'\eta - (2k_x^2 + k_z^2)\eta(1-\eta) - 1 \\ \mathrm{i}k_x\eta - 2\mathrm{i}k_x(1-\eta) \\ -k_xk_z\eta(1-\eta) \end{pmatrix}, \tag{4.12}$$

$$\boldsymbol{R}_1 = \begin{pmatrix} 0 \\ \mathrm{i}k_xU_0' \\ 0 \\ -\mathrm{i}k_xU_0U_0' - (2k_x^2 + k_z^2)(1-\eta) \\ \mathrm{i}k_x \\ -k_xk_z(1-\eta) \end{pmatrix}. \tag{4.13}$$

The general solution of the linear differential system (4.9) reads

$$\mathbf{Z}_1 = c_1^{(1)}\mathbf{Z}_1^{(1)} + c_1^{(2)}\mathbf{Z}_1^{(2)} + c_1^{(3)}\mathbf{Z}_1^{(3)} + D_1\mathbf{Z}_1^{(D)} + R_1\mathbf{Z}_1^{(R)}. \tag{4.14}$$

Thus, $\mathbf{Z}_1$ is expressed as the superposition of three linearly independent solutions of the homogeneous problem

$$\mathscr{L}\mathbf{Z}_1^{(1,2,3)} = 0, \tag{4.15}$$

which satisfy the boundary conditions at the lower boundary, plus particular solutions of the non-homogeneous differential systems

$$\mathscr{L}\mathbf{Z}_1^{(D)} = \boldsymbol{D}_1, \quad \mathscr{L}\mathbf{Z}_1^{(R)} = \boldsymbol{R}_1, \tag{4.16}$$

again satisfying the lower boundary conditions. Without loss of generality, the constants $c_1^{(1)}$, $c_1^{(2)}$ and $c_1^{(3)}$ are chosen so as to represent the amplitudes of the perturbed tangential, normal and binormal stresses at the reference level, respectively.

Using the splitting (4.14) in the linearized boundary conditions at the free surface (3.5), the following complex algebraic non-homogeneous system in the four unknowns:

$$\boldsymbol{C}_1 = (c_1^{(1)}, c_1^{(2)}, c_1^{(3)}, D_1)^{\mathrm{T}}, \tag{4.17}$$

is found in the form

$$\boldsymbol{F}_1 \cdot \boldsymbol{C}_1 = -R_1 \boldsymbol{f}_1, \tag{4.18}$$

where the matrix $\boldsymbol{F}_1$ and the vector $\boldsymbol{f}_1$ read

$$\boldsymbol{F}_1 = \begin{bmatrix} V_1^{(1)} & V_1^{(2)} & V_1^{(3)} & V_1^{(D)} - \mathrm{i}k_x U_0 \\ T_{t1}^{(1)} & T_{t1}^{(2)} & T_{t1}^{(3)} & T_{t1}^{(D)} \\ T_{n1}^{(1)} & T_{n1}^{(2)} & T_{n1}^{(3)} & T_{n1}^{(D)} + S^{-1} \\ T_{b1}^{(1)} & T_{b1}^{(2)} & T_{b1}^{(3)} & T_{b1}^{(D)} \end{bmatrix}_{\eta=1}, \quad \boldsymbol{f}_1 = \begin{bmatrix} V_1^{(R)} - \mathrm{i}k_x U_0 \\ T_{t1}^{(R)} \\ T_{n1}^{(R)} + S^{-1} \\ T_{b1}^{(R)} \end{bmatrix}_{\eta=1}. \tag{4.19}$$

The solution of the system (4.18) is proportional to R_1 so that $\boldsymbol{Z}_1$ can be set equal to $R_1 \boldsymbol{X}_1$, the vector $\boldsymbol{X}_1$ providing the forced response of the flow to a unit bed perturbation.

Substituting the solution $\boldsymbol{X}_1$ into the linearized sediment continuity equation (3.8) yields the following dispersion relationship:

$$\Omega(1 + L_1) = Qk_x \left[A_{x0} \left(\frac{T_{t1B}}{k_x} - \mathrm{i}\frac{\mu_x}{\theta_0} \right) + A_{z0} \frac{k_z^2}{k_x^2} \left(\frac{T_{b1B}}{k_z} - \mathrm{i}\frac{\mu_z \sqrt{\theta_{B0}}}{\theta_0} \right) \right], \tag{4.20}$$

where T_{t1B} and T_{b1B} are the perturbations of the tangential and binormal shear stresses evaluated at the level B_0, respectively. Moreover, the term L_1, which represents the perturbation of the bedload layer thickness, is obtained by linearization of (3.12) and reads

$$L_1 = \frac{A_{L0}\theta_{B0}(T_{t1R} - \mathrm{i}k_x \mu_x / \theta_{C0})}{1 + A_{L0}\theta_0}. \tag{4.21}$$

Note that, in our previous works, L was not perturbed, since the correction of the growth rate associated with L_1 was minimal. When moving to larger values of d_s, we found that this correction assumed an increased importance, ultimately leading to the disappearance of the antidune mode for very low values of the conductance coefficient C, in line with experimental observations. On the contrary, bar and dune modes are almost unaffected by this correction, since h_{s0}, and thus A_{L0}, tends to vanish for low values of the Shields parameter.

Equation (4.20) allows for the determination of the growth rate Ω^G and wave celerity Ω^C of the bed perturbation as a function of the longitudinal and transverse wavenumbers k_x and k_z and of two parameters, one chosen among θ_0 and Fr, the other among C and d_s. In fact, the former are related by (2.3) and the latter by (2.1).

In particular, we have

$$\Omega^G = k_x \frac{\mathrm{Im}(\Omega)}{C}, \quad \Omega^C = \frac{\mathrm{Re}(\Omega)}{C}, \tag{4.22}$$

where a division by C has been introduced to scale with the flow time scale D^*/U^*.

Finally, note that if k_z is set equal to zero in (4.20), the classical balance between the streamwise bed shear stress and the stabilizing effect of gravity that leads to dune and antidune formation is recovered. The term proportional to A_{z0}, which displays a similar structure, is thus to be held responsible for three-dimensional effects.

5. Discussion of results

We start our discussion by focusing on two ideal experiments that are performed in order to explain the appearance (and disappearance) of two- and three-dimensional bed forms as the relevant flow and sediment parameters are changed. In all the configurations analysed, the bed is assumed to be composed by sediments of the same dimensional grain size.

In the first ideal experiment, we aim at the transition from two-dimensional dunes to alternate bars, which is observed as the conductance coefficient C is lowered for a constant, relatively low, value of the Shields parameter. Moreover, antidunes will be shown to appear as the Shields parameter is increased at constant values of C. To this end, we first explore the stability maps obtained for several decreasing values of the conductance coefficient C at the same θ. Secondly, for the lowest value of C considered, the Shields parameter is increased, which corresponds to an increase of the Froude number.

Note that, by this choice, the dimensional flow depth is constant in each map, so that variations in the transverse wavenumber k_z, which, by definition, is inversely proportional to the width-to-depth ratio β, correspond to a change of the channel width.

The stability maps relative to this first ideal experiment are shown in figure 3, where the growth rate Ω^G is plotted in shades of grey in the space of the streamwise and spanwise wavenumbers, lighter colours corresponding to (positive) larger values. The contour lines are chosen on a logarithmic scale, so that

$$\Omega^G = \{0, \pm 10^{-6}, \pm 10^{-5.5}, \pm 10^{-5}, \pm 10^{-4.5}, \ldots\}. \tag{5.1}$$

The white solid lines indicate marginal stability, i.e. $\Omega^G = 0$, and bound the regions of instability.

Moving from panel (*a*) to panel (*d*), it can be seen how the most unstable mode, which initially lies on the horizontal axis, becomes three-dimensional as C decreases. This is related to the fact that two-dimensional dunes become stable as C is lowered. Moreover, the longitudinal wavenumber of maximum amplification decreases from values of $O(1)$, typical of dunes, to values of $O(10^{-2})$, typical of alternate bars (see figure 1*b*). Note that, owing to (2.1), a decrease in C corresponds to an exponential decrease of flow depth. Moreover, in order to keep constant the value of the Shields parameter, the area velocity must decrease as well, whereas the Froude number increases following (2.3).

The stability plots shown in figure 3(*d–f*) have been obtained for the same value of C but with increasing values of the Shields parameter and thus of the Froude number. By comparison, it can be seen how Fr has a limited influence on the bar mode, which only slightly contracts, thus confirming the observation that alternate bars are quite insensitive to variations of the flow regime. On the contrary, an increase in the Froude number leads to the appearance of the antidune mode, which progressively becomes the most unstable. A tendency to form three-dimensional antidunes is also shown in the last panel.

It can be concluded that, accordingly with observations, the parameter that controls the transition from two-dimensional dunes to alternate bars is the conductance coefficient C or else the non-dimensional grain size d_s. Although, owing to (2.3), the Froude number increases as C is lowered, its role in this regard is subordinate. On the contrary, for any given value of C, an increase in the Froude number leads to the appearance of the antidune mode associated with the transition from the sub- to the

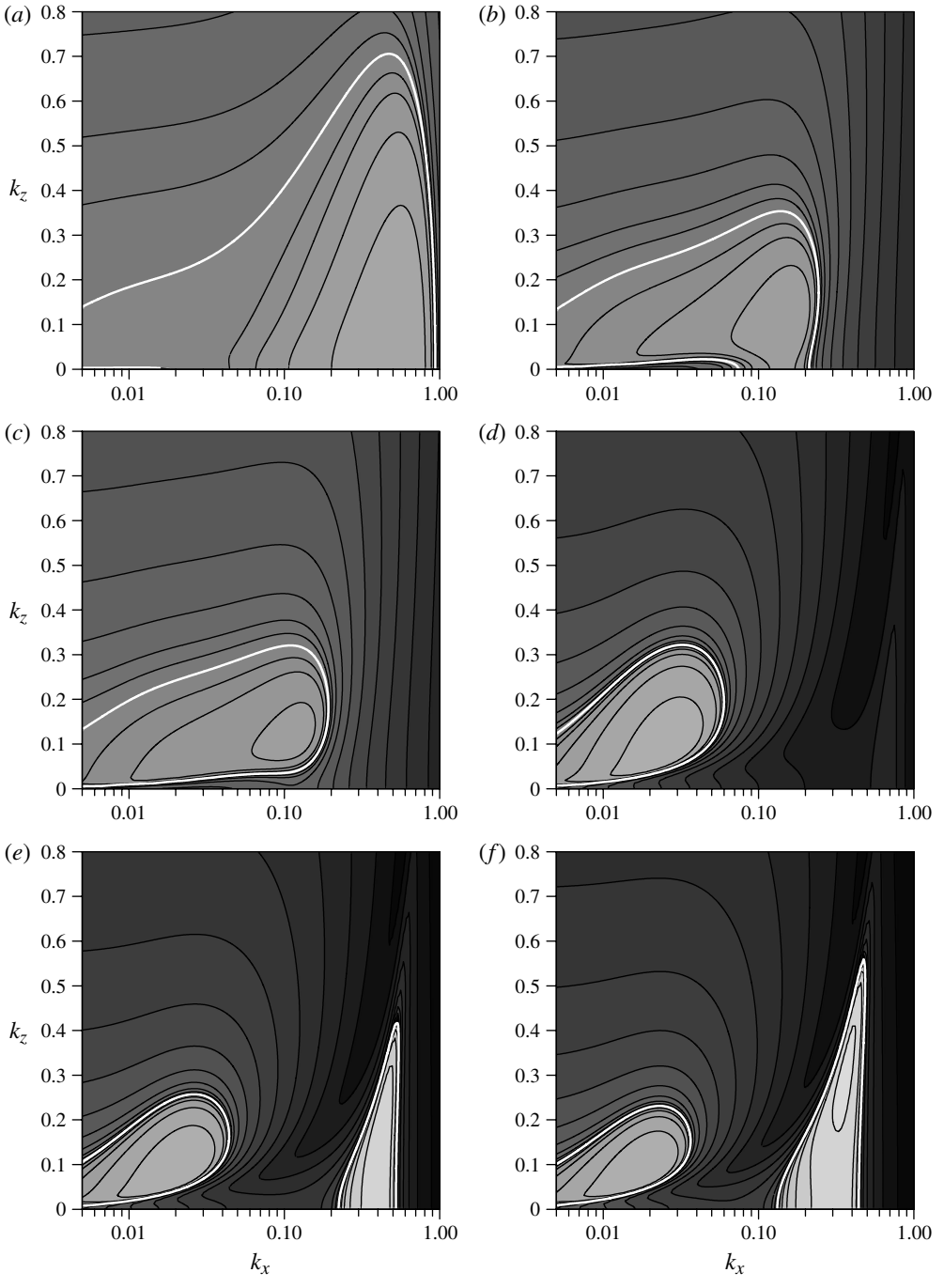

FIGURE 3. Stability plots at $\theta/\theta_C = 2$: (*a*) $C = 19$, (*b*) $C = 15.5$, (*c*) $C = 15$ and at $C = 10$: (*d*) $\theta/\theta_C = 2$, (*e*) $\theta/\theta_C = 3$, (*f*) $\theta/\theta_C = 4$.

supercritical regime. Note that the regions of instability of bars and antidunes remain distinct. Hence, antidunes and bars do linearly coexist, the former being dominant over the latter at high values of the Shields parameter and *vice versa*.

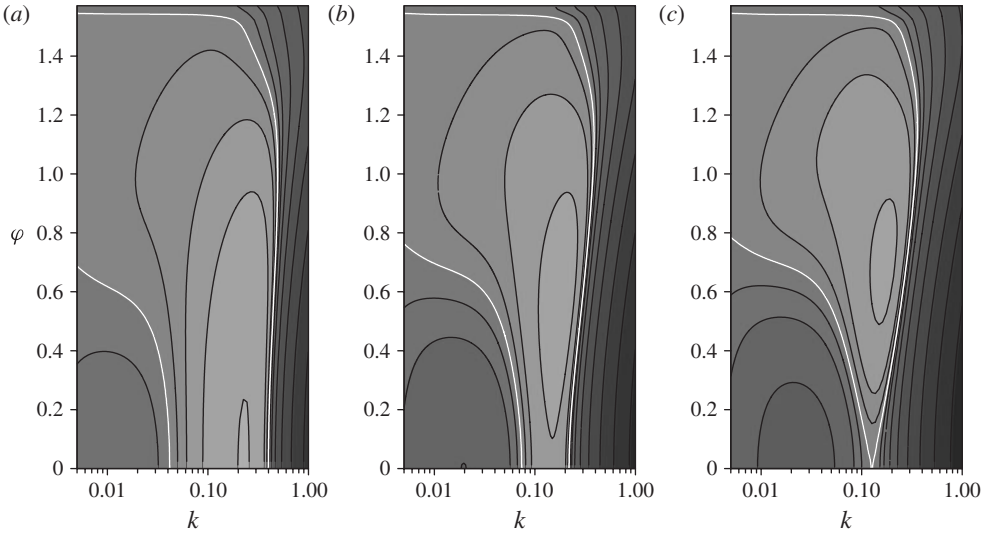

FIGURE 4. Stability plots in the (k, φ) plane for $\theta/\theta_C = 2$ and: (a) $C = 16.5$; (b) $C = 15.5$; (c) $C = 15.185$.

We remark that the above considerations cannot be drawn in the framework of shallow-water flow models previously adopted for the study of alternate bar formation, since the dynamics of dunes and antidunes, which are typically much shorter than bars, is not correctly grasped by depth-averaged models (Reynolds 1976).

It is also interesting to note that the transition from two- to three-dimensional dunes is characterized by a single maximum. In fact, having defined the wave-vector norm k and its angle φ with respect to the longitudinal axis as

$$k = \sqrt{k_x^2 + k_z^2}, \quad \tan\varphi = \frac{k_z}{k_x} \tag{5.2}$$

it can be proved that, for any finite k,

$$\lim_{\varphi \to 0} \frac{\partial \Omega^G}{\partial \varphi} = 0, \tag{5.3}$$

so that the most unstable two-dimensional mode, which is characterized by a vanishing derivative of the growth rate in the k-direction and lies on the horizontal axis, is, in the φ-direction, either a maximum, as shown in figure 4(a), or a minimum, as shown in figures 4(b) and 4(c), the last one corresponding to the peculiar situation of marginal instability for the two-dimensional disturbance.

As a consequence, the transition from two-dimensional dunes to alternate bars is also characterized by a single maximum, so that it can be concluded that, opposite to the antidune-bar case, alternate bars and dunes never coexist at a linear level.

An important theoretical result is displayed in figure 4(b,c): in these configurations, three-dimensional disturbances are more unstable than their two-dimensional counterparts. Therefore, as argued by Seminara (2010), no 'Squire theorem' analogy can be cast for the linear stability of dunes, as opposite to the classical result obtained for purely hydrodynamic stability. We strongly believe that this result is of more general value and can be extended to any morphodynamic problem.

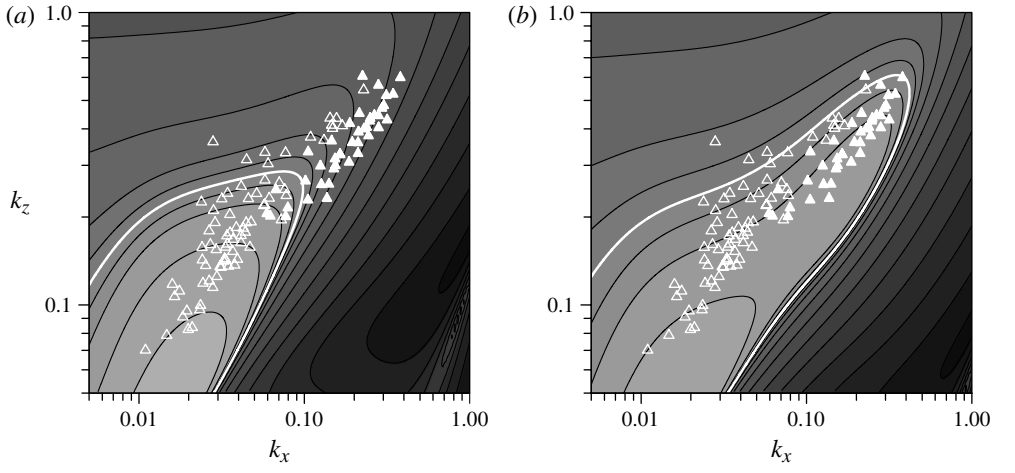

FIGURE 5. Stability plots at $\theta/\theta_C = 2.2$: (*a*) narrower channel, $Z_B = 800$; (*b*) wider channel, $Z_B = 1600$. Symbols denote experimental runs of alternate (hollow) and diagonal (solid) bars from the JSM data set.

The second ideal experiment aims at the distinction between alternate and diagonal bars. We intend to show that diagonal bars are indeed to be considered as three-dimensional dunes, thus explaining their different observed behaviours and wavelengths with respect to alternate bars. To this end, we consider the stability maps for two channels, one half as wide as the other, for the same value of the Shields parameter. The flow depth is also halved, so that the width-to-depth ratio β remains unchanged. Note that, by this choice, the dimensional flow depth linearly increases in each map with k_z, whereas d_s decreases (and so C increases). Note also that the double-periodic perturbation (4.1) can be thought of as representative of the flow in a channel of width equal to one-half of the transverse wavelength, provided that the width-to-depth ratio β is large enough to allow for neglecting the effect of the wall layers at the channel banks.

Considering the results for the narrower configuration, shown in figure 5(*a*), it appears that the unstable region can be associated with alternate bars. In fact, most of the corresponding experimental runs (hollow markers) fall inside the region, following quite closely the line of maximum amplification. Indeed, if turned upside down, the classical U-shaped marginal stability curve for bar instability is recovered (Blondeaux & Seminara 1985; Colombini *et al.* 1987, among others), showing how the width-to-depth ratio β controls the onset of instability. In fact, a 'critical' value of β, which corresponds to the maximum in k_z of the marginal curve in figure 5(*a*), is easily detected.

Increasing the channel width, as shown in figure 5(*b*), leads to a modification of the marginal curve, which extends to cover shorter longitudinal and transverse wavelengths, nicely including most of the experimental observations on diagonal bars, reported in the plot as solid markers.

Therefore, the present results suggest that increasing the channel width, while keeping constant the Shields parameter and the sediment grain size, leads to the formation of diagonal bars. This is consistent with the criterion for alternate bar formation introduced by Jaeggi (1984), given by (2.6). In fact, the stability diagrams shown in figure 5 represent two configurations whereby, for each value of β, Z_B

doubles in moving from the narrower to the wider channel, whereas all the other quantities appearing in (2.6) remain constant. As a consequence, the left-hand side of (2.6) increases, leading to the appearance of diagonal bars, as predicted by the present theory.

For both alternate and diagonal bars, a fairly good agreement is found between the wavenumbers of maximum amplification and the experimental observations. We point out that all the experimental runs considered were relative to mature bed forms. Hence, as in the case of two-dimensional dunes and antidunes, linear analyses seem to be able to correctly grasp the information on wavelengths, thus suggesting that bed form wavelengths settle during the linear phase. Coarsening phenomena that have been observed during the initial phase of formation for both bars and dunes remain unexplained by the present analysis. However, the recent work of Camporeale & Ridolfi (2011) might provide an explanation of this apparent contradiction, whereby coarsening is associated with the appearance of shorter transient features, still in the linear regime, which disappears at longer times when the wavelengths selected by the normal analysis are recovered.

6. Conclusions

In the present contribution, a linear stability analysis is presented, whereby the flow and the sediment transport models previously developed to study the formation of two-dimensional bed forms have been extended to cover variations in the transverse direction. Depending on the values of the relevant flow and sediment parameters, several regions of instability appear that can be associated with a variety of bed forms, spanning from two-dimensional dunes and antidunes to alternate bars through diagonal bars and three-dimensional dunes and antidunes.

At low values of the Shields parameter, the most unstable pattern, corresponding to two-dimensional dunes for larger depths, is shown to progressively lose stability towards three-dimensional configurations as the flow becomes shallower. If the depth is further decreased, two-dimensional disturbances become linearly stable and bars are left as the only unstable pattern. For higher values of θ, the formation of two- and three-dimensional antidunes is predicted.

A comprehensive picture of the formation of two- and three-dimensional bed forms emerges from the present analysis, showing the role of two relevant parameters: the conductance coefficient and the Froude number. The former controls the transition from two- to three-dimensional dunes and, then, to alternate bars, the latter the transition from bars and dunes to antidunes.

Under suitable conditions, three-dimensional configurations are found to be more unstable than their two-dimensional counterparts, thus proving that, in contrast with a classical result for hydrodynamic instability, a morphodynamic Squire theorem does not hold.

The crucial role of the width-to-depth ratio β for the formation of alternate bars, already outlined by previous theories based on the shallow-water approximation, is confirmed. Moreover, the present theory, which accounts for the role of flow depth, is able to well describe the linear competitions among the dune, antidune and bar modes and provides an explanation of the different observed behaviours of alternate and diagonal bars, the latter being identified as three-dimensional dunes expressing a single alternating diagonal front. These aspects could not be adequately described in the framework of shallow-water models.

Finally, we remark that the present work, although limited to a linear framework, might provide a first answer to the 'urgent need to understand the complex relationships between bed form three-dimensionality and the associated flow field, and the role of three-dimensionality in modulating both flow and sediment transport' expressed by Best (2005) in his state-of-the-art review of the fluid dynamics of river dunes.

REFERENCES

ALLEN, J. R. L. 1982 *Sedimentary Structures: Their Character and Physical Basis – Vol. 1*. Elsevier.

ASCE, TASK COMMITTEE, 1963 Friction factors in open channels. *J. Hydraul. Div. ASCE* **89** (HY2), 97–143.

BESIO, G., BLONDEAUX, P. & VITTORI, G. 2006 On the formation of sand waves and sand banks. *J. Fluid Mech.* **557**, 1–27.

BEST, J. 2005 The fluid dynamics of river dunes: a review and some future research directions. *J. Geophys. Res. – Earth Surface* **110**, F04S02.

BLONDEAUX, P. & SEMINARA, G. 1985 A unified bar-bend theory of river meanders. *J. Fluid Mech.* **157**, 449–470.

BLONDEAUX, P. & VITTORI, G. 2011 Dunes and alternate bars in tidal channels. *J. Fluid Mech.* **670**, 558–580.

CALLANDER, R. A. 1969 Instability and river channels. *J. Fluid Mech.* **36**, 465–480.

CAMPOREALE, C. & RIDOLFI, L. 2011 Modal versus nonmodal linear stability analysis of river dunes. *Phys. Fluids* **23** (10), 104102.

COLOMBINI, M. 2004 Revisiting the linear theory of sand dune formation. *J. Fluid Mech.* **502**, 1–16.

COLOMBINI, M., SEMINARA, G. & TUBINO, M. 1987 Finite-amplitude alternate bars. *J. Fluid Mech.* **181**, 213–232.

COLOMBINI, M. & STOCCHINO, A. 2005 Coupling or decoupling bed and flow dynamics: fast and slow sediment waves at high Froude numbers. *Phys. Fluids* **17** (3), 9.

COLOMBINI, M. & STOCCHINO, A. 2008 Finite-amplitude river dunes. *J. Fluid Mech.* **611**, 283–306.

COLOMBINI, M. & STOCCHINO, A. 2011 Ripple and dune formation in rivers. *J. Fluid Mech.* **673**, 121–131.

DEVAUCHELLE, O., MALVERTI, L., LAJEUNESSE, È., LAGRÈE, P.-Y., JOSSERAND, C. & NGUYEN THU-LAM, K.-D. 2010 Stability of bedform in laminar flows with free-surface: from bars to ripples. *J. Fluid Mech.* **642**, 329–348.

EINSTEIN, H. A. & SHEN, H. W. 1964 A study on meandering in straight alluvial channels. *J. Geophys. Res.* **69**, 5239–5247.

ENGELUND, F. 1970 Instability of erodible beds. *J. Fluid Mech.* **42**, 225–244.

ENGELUND, F. 1974 The development of oblique dunes. *Prog. Rep.* 1–2. Technical University of Denmark, Institute of Hydrodynamics and Hydraulic Engineering.

ENGELUND, F. 1981 The motion of sediment particles on an inclined bed. *ISVA Prog.* 53. Technical University of Denmark, Institute of Hydrodynamics and Hydraulic Engineering.

ENGELUND, F. & FREDSØE, J. 1974 Transition from dunes to plane bed in alluvial channels. *Series paper* 4. Technical University of Denmark, Institute of Hydrodynamics and Hydraulic Engineering.

FREDSØE, J. 1974*a* The development of oblique dunes. *Prog. Rep.* 3–4. Technical University of Denmark, Institute of Hydrodynamics and Hydraulic Engineering.

FREDSØE, J. 1974*b* On the development of dunes in erodible channels. *J. Fluid Mech.* **64**, 1–16.

GRADOWCZYK, M. H. 1968 Wave propagation and boundary instability in erodible-bed channels. *J. Fluid Mech.* **33**, 93–112.

GUY, H. P., SIMONS, D. B. & RICHARDSON, E. V. 1966 Summary of alluvial channel data from flume experiments 1956–61. *Prof. paper* 462-I. US Geological Survey.

HALL, P. 2006 Nonlinear evolution equations and the braiding of weakly transporting flows over gravel beds. *Stud. Appl. Maths* **117**, 27–69.

IDIER, D. & ASTRUC, D. 2003 Analytical and numerical modelling of sandbanks dynamics. *J. Geophys. Res. – Oceans* **108**, 3060–3074.

JAEGGI, M. 1984 Formation and effects of alternate bars. *J. Hydraul. Engng. ASCE* **110**, 142–156.

KENNEDY, J. F. 1963 The mechanism of dunes and antidunes in erodible-bed channels. *J. Fluid Mech.* **16**, 521–544.

LAJEUNESSE, E., MALVERTI, L., LANCIEN, P., ARMSTRONG, L., MÉTIVIER, F., COLEMAN, S., SMITH, C. E., DAVIES, T., CANTELLI, A. & PARKER, G. 2010 Fluvial and submarine morphodynamics of laminar and near-laminar flows: a synthesis. *Sedimentology* **57**, 1–26.

MEYER-PETER, E. & MÜLLER, R. 1948 Formulas for bed-load transport. In *Proceedings of 2nd IAHR Meeting*, pp. 39–64. Stockholm, Sweden.

MURAMOTO, Y. & FUJITA, Y. 1978 The classification of meso-scale river bed configuration and the criterion of its formation. In *Proceedings of 22nd Japanese Conference on Hydraulics, Japan*, pp. 275–282.

REYNOLDS, A. J. 1976 A decade's investigation of the stability of erodible stream beds. *Nord. Hydrol.* **7**, 161–183.

ROOS, P. C., HULSCHER, S. J. M. H., KNAAPEN, M. A. F. & VAN DAMME, R. M. J. 2004 The cross-sectional shape of tidal sandbanks: modelling and observations. *J. Geophys. Res. – Earth Surface* **109**, F02003.

SEMINARA, G. 2010 Fluvial sedimentary patterns. *Annu. Rev. Fluid Mech.* **42**, 43–66.

SEMINARA, G., SOLARI, L. & PARKER, G. 2002 Bed load at low Shield stress on arbitrarily sloping beds: failure of the Bagnold hypothesis. *Water Resour. Res.* **38**, W000681.

SUKEGAWA, N. 1971 Study on meandering of streams in straight channels. *Tech. Rep.* Bureau of Resources, Department of Science & Technology, Japan.

TUBINO, M., REPETTO, R. & ZOLEZZI, G. 1999 Free bars in rivers. *J. Hydraul. Res.* **32**, 759–775.

WONG, M. & PARKER, G. 2006 Reanalysis and correction of bed-load relation of Meyer–Peter and Müller using their own database. *J. Hydraul. Engng. ASCE* **132**, 1159–1168.